Adaptive multilevel space-time-stepping scheme for transport in heterogeneous porous media (ADM-LTS)

Carciopolo, Ludovica Delpopolo; Cusini, Matteo; Formaggia, Luca; Hajibeygi, Hadi

DOI
10.1016/j.jcpx.2020.100052

Publication date
2020

Document Version
Final published version

Published in
Journal of Computational Physics: X

Journal of Computational Physics: X 6 (2020) 100052

Contents lists available at ScienceDirect

Journal of Computational Physics: X

www.elsevier.com/locate/jcpx

Adaptive multilevel space-time-stepping scheme for transport in heterogeneous porous media (ADM-LTS)

Ludovica Delpopolo Carciopolo [a,*], Matteo Cusini [b], Luca Formaggia [a], Hadi Hajibeygi [c]

[a] MOX, Dipartimento di Matematica, Politecnico di Milano, Via Bonardi 9, 20133 Milano, Italy
[b] Atmospheric, Earth, & Energy Division, Lawrence Livermore National Laboratory, 7000 East Ave., Livermore, CA 94550-9234, United States of America
[c] Department of Geoscience and Engineering, Faculty of Civil Engineering and Geosciences, Delft University of Technology, Stevinweg 1, 2628 CN, Delft, the Netherlands

ARTICLE INFO

Article history:
Received 11 June 2019
Received in revised form 10 February 2020
Accepted 19 February 2020
Available online 3 March 2020

Keywords:
Local time-stepping strategies
Conservative multirate methods
Algebraic multilevel methods
Multiphase flow
Porous media

ABSTRACT

We present ADM-LTS, an adaptive multilevel space-time-stepping scheme for transport in heterogeneous porous media. At each time step, firstly, the flow (pressure) solution is obtained. Then, the transport equation is solved using the ADM-LTS method, which consists of two stages. In the first stage, an initial solution is obtained by imposing the coarsest space-time grid. This initial solution is then improved, in the second stage, by imposing a space-time adaptive grid on the cells where the solution does not satisfy the desired quality. The quality control is based on error estimators with user-defined threshold values. The time-integration procedure, in which the coarsest-scale solution provides local flux boundary conditions for sub-domains with local time refinement, is strictly mass conservative. In addition, the method employs space-time fine grid cells only at the moving saturation fronts. In order to ensure local mass conservation at all levels, finite-volume restriction operators and unity prolongation operators are developed. Several numerical experiments have been performed to analyze the efficiency and accuracy of the proposed ADM-LTS method for both homogeneous and heterogeneous permeability fields on two and three dimensional domains. The results show that the method provides accurate solutions, at the same time it maintains the computational efficiency. The ADM-LTS implementation is publicly available at https://gitlab.com/darsim2simulator.

1. Introduction

Simulation of transport in natural porous media is challenging due to the variety of time and length scales involved in the process. In fact, geological formations extend several hundreds of meters whereas physical and chemical phenomena, which are relevant in many applications (e.g., energy and greenhouse gas storage and geo-energy production), occur at much smaller scales (cm and below). Additionally, at the continuum (or Darcy) scale, porous media present highly heterogeneous discrete properties (e.g., permeability) with no separation of scales. This leads to having fast and slow transport processes

* Corresponding author.
E-mail addresses: ludovica.delpopolo@polimi.it (L. Delpopolo Carciopolo), cusini1@llnl.gov (M. Cusini), luca.formaggia@polimi.it (L. Formaggia), H.Hajibeygi@tudelft.nl (H. Hajibeygi).

https://doi.org/10.1016/j.jcpx.2020.100052

coexist in one computational domain. Accurate numerical models, thus, require very high resolution grids both in space and time to capture all relevant physics. However, due to the big size of the domains and the large number of simulations for uncertainty reduction [1,2], field-scale simulations on such high resolution grids are impractical.

The global system complexity cannot be reduced by upscaling approaches, as the heterogeneous properties often times do not entail clear separation of scales [3]. Alternatively, one can map scalable part of the solution (e.g. pressure) in coarser spatial resolutions, as in the multiscale methods [4–8]. For the transport (e.g. saturation) equation, due to its local nature, Adaptive Mesh Refinement (AMR) schemes provide a promising framework for the reduction of the computational complexity [9,10]. Both approaches address resolution challenges in space only, which can be integrated into an operator-based strategy by the Algebraic Dynamic Multilevel (ADM) method [11,12].

ADM maps the spatial fine-scale system into a dynamic multilevel system by using sequences of local operators (restriction and prolongation). It can be applied to coupled flow-transport, or only transport equation. In addition to explicit and implicit time integration schemes, both sequential and fully-implicit coupling strategies can be treated in a straightforward manner. The focus of the present study is on the transport equation, which is sequentially coupled with the pressure and velocity solver at each time step.

Similar to AMR, ADM develops an adaptive spatial-grid stepping scheme. In contrast to AMR, however, ADM is applicable to heterogeneous systems without dependency on upscaling parameters.

Although important, spatial grid is only part of the full transport simulation advancement. To further advance the overall simulation efficiency, one may need to take large time step sizes. However, the excessive numerical dispersion introduced by the use of large time steps can significantly impact the accuracy of the solution, e.g., by smearing the advancing saturation front. It is therefore crucially important to, not only allow for large time step sizes, but also to control the accuracy by resolving the sharp fronts using smaller time steps. Such a development is made possible–for static spatial grids–by Local Time Stepping (LTS) or multirate methods [13]. Recent LTS methods allow for self-adjusting time-stepping strategies based on a posteriori error estimator [14] in a strictly conservative implicit time integration framework [15]. The LTS for conservative transport simulation on fine-scale spatial grid has been also successfully integrated with the pressure solver of the multiscale finite volume method [16]. This idea was also followed to develop an explicit LTS scheme [17]. Note that all of these mentioned methods depend on a given static single-level spatial grid for transport.

Of particular interest is to develop an adaptive space-time stepping scheme for transport simulation. This development would allow not only to adjust the spatial, but also temporal grid in order to achieve the optimum efficient and accurate transport solutions.

In this paper, the adaptive space-time stepping scheme (ADM-LTS) is devised. This new development makes it possible to march adaptively both in space and time (with an arbitrary number of levels) to obtain accurate and efficient solutions for complex transport in heterogeneous porous media. Additionally, the proposed ADM-LTS method preserves mass conservation, even though it takes different time step sizes in different subsets of the domain. This is made possible by obtaining an initial solution estimator on the coarsest space-time grid, and impose it as Neumann (fixed flux) boundary condition to local regions with smaller space-time steps.

Note that the ADM-LTS is developed for the transport equation, within the coupled flow-transport multiphase simulation. In particular, it is emphasized that the pressure equation solution is assumed to be available by any advanced solver, which stays out of the scope of this paper. Once the pressure and velocity fields are obtained, ADM-LTS is imposed on the transport equation, with adaptive space-time grid based on space-time error estimators. As a consequence, the method is able to use a fine-grid resolution (in space and time) only at the location of the moving saturation fronts. More precisely, the method first applies a global time step on the coarsest possible grid resolution. Then, it defines a multilevel grid resolution on the basis on the error estimators. On this new grid, the solution is recomputed with smaller time steps only in a fraction of the domain.

ADM-LTS is different, yet complementary, to other advanced methods for transport equation, specially the Adaptive Implicit Method (AIM) [18–20]. AIM develops an adaptive implicit-explicit time-integration scheme, but takes the same space-time grids everywhere. ADM-LTS, on the other hand, is developed to allow different space and time step sizes in a domain, irrespective of the choice of the time-integration scheme.

The ADM-LTS method is applied to homogeneous and heterogeneous 2D and 3D test cases including complex nonlinear transport physics (i.e., gravitational forces and capillarity heterogeneity). Systematic studies of the performance (i.e., accuracy and system complexity) are presented. Numerical test cases show that the ADM-LTS approach provides an accurate solution reducing the number of active cells both in space and in time.

The paper is organized as follows. The equations describing multiphase flow in porous media are presented in section 2 along with the fine-scale discrete systems for transport equation. The ADM-LTS method is explained in detail in section 3 whereas numerical experiments are presented in section 4. Finally, conclusions are provided in section 5.

2. Sequential-implicit simulation

Mass conservation equations for the flow of N_p incompressible phases in a d-dimensional porous domain $\Omega \subset \mathbb{R}^d$ read

$$\frac{\partial}{\partial t}(\phi \rho_\alpha S_\alpha) + \nabla \cdot (\rho_\alpha \boldsymbol{u}_\alpha) = q_\alpha \qquad \forall \alpha \in \{1, \dots, N_p\}. \tag{1}$$

Here, S_α, ρ_α and q_α are the α-phase saturation, density and source term (i.e., wells). The Darcy velocity for α-phase can be written as

$$\boldsymbol{u}_\alpha = -\mathbf{K}\lambda_\alpha \left(\nabla p_\alpha + \rho_\alpha g \nabla z\right) \qquad \forall \alpha \in \{1, \dots, N_p\}. \tag{2}$$

Here, the phase mobility is denoted by λ_α, and $\lambda_\alpha = k_{r\alpha}/\mu_\alpha$ holds, where $k_{r\alpha}$ and μ_α are the phase relative permeability and viscosity, respectively. Furthermore, $\mathbf{K}$ is the rock absolute permeability (defined at discrete fine-scale resolution). Additionally, p_α are the phase pressures, which are related to the capillary pressure P_c as

$$p_\alpha - p_\beta = (1 - \delta_{\alpha,\beta}) P_{c_{\alpha,\beta}} \qquad \forall \alpha, \beta \in \{1, \dots, N_p\}. \tag{3}$$

Here, $\delta_{\alpha,\beta}$ is the Kronecker delta, which is equal to 1 if $\alpha = \beta$ and 0 otherwise, while $P_{c_{\alpha,\beta}}$ is a nonlinear function of wetting phase saturation. Note that the constraint $\sum_{\alpha=1}^{N_p} S_\alpha = 1$ allows for eliminating one of the unknowns. Assuming incompressible fluids and rock, in a two-phase system one can use the non wetting (nw) pressure and the wetting (w) saturation as primary variables [21,22]. We will then set $p = p_{nw}$, $S = S_w$ and define a total velocity as

$$\boldsymbol{u}_t = \boldsymbol{u}_{nw} + \boldsymbol{u}_w. \tag{4}$$

Sequential-implicit simulation requires a decoupled pressure-saturation sets of equations. The equation for pressure is obtained by combining the mass-balance equations, to have

$$\nabla \cdot \boldsymbol{u}_t = \frac{q_w}{\rho_w} + \frac{q_{nw}}{\rho_{nw}} \qquad \text{in } \Omega, \tag{5}$$

where the total velocity is expressed as

$$\boldsymbol{u}_t = \mathbf{K}\Big(-\lambda_t \nabla p + \lambda_w \nabla P_c - (\lambda_w \rho_w + \lambda_{nw}\rho_{nw}) g \nabla z\Big). \tag{6}$$

On the other hand, the (wetting-phase) saturation equation is re-written by introducing the fractional flow function $f_w = \lambda_w/\lambda_t$, thus obtaining

$$\frac{\partial(\phi S)}{\partial t} + \nabla \cdot \Big\{\mathbf{K} f_w \lambda_{nw} \left(\nabla P_c + (\rho_{nw} - \rho_w) g \nabla z\right) + f_w \boldsymbol{u}_t\Big\} = \frac{q_w}{\rho_w} \qquad \text{in } \Omega. \tag{7}$$

Equations (5), (6) and (7) are coupled by the total velocity, the (nonlinear) phase relative permeability $k_{r\alpha}$ and the capillary pressure P_c.

Sequential implicit simulation (SIM) consists of decoupling the pressure and transport equations at numerical level, and solving each of them implicitly in time. Given the state at a current time t^n, the solution at time t^{n+1} is found by first solving Eq. (5), freezing all saturation dependencies, i.e.,

$$-\nabla \cdot \left(\mathbf{K}\lambda_t^n \nabla p^{n+1}\right) = q_t - \nabla \cdot \left(\mathbf{K}(\lambda_w^n \nabla P_c^n - (\lambda_w^n \rho_w + \lambda_{nw}^n \rho_{nw}) g \nabla z)\right), \tag{8}$$

where $q_t = q_w/\rho_w + q_{nw}/\rho_{nw}$. Then, the total velocity is computed as

$$\boldsymbol{u}_t^{n+1} = -\mathbf{K}\left(\lambda_t^n \nabla p^{n+1} - \lambda_w^n \nabla P_c^n + (\lambda_w^n \rho_w + \lambda_{nw}^n \rho_{nw}) g \nabla z\right). \tag{9}$$

Finally the transport equation is solved, i.e.,

$$\begin{aligned} &\phi \frac{S^{n+1} - S^n}{\Delta t} + \\ &\nabla \cdot \left(\mathbf{K} f_w^{n+1} \lambda_{nw}^{n+1} \left(\nabla P_c^{n+1} + (\rho_{nw} - \rho_w) g \nabla z\right) + f_w^{n+1} \boldsymbol{u}_t^{n+1}\right) - \frac{q_w}{\rho_w}^{n+1} = 0. \end{aligned} \tag{10}$$

The saturation equation is a nonlinear function. Thus, we employ a Newton-Raphson's method for Eq. (10), which leads to a sequence of systems of the form $\mathsf{J}^\nu \delta \mathsf{x}^{\nu+1} = -\mathsf{r}^\nu$. Here, $\delta \mathsf{x}$ is the vector of increment for saturation, J is the Jacobian matrix, r is the residual, and ν the iteration index.

For each cell K, one can write the residual as

$$\mathsf{r}_K^{n+1} = \phi(S_K^{n+1} - S_K^n) - \frac{1}{|K|} \sum_{e_{KL} \in \mathcal{E}_K} e_{KL} F_{KL}^{n+1} - \frac{q_w}{\rho_w}^{n+1} = 0. \tag{11}$$

Here, $|K|$ is the volume of element K, e_{KL} the area of the interface between cells K and L and $\mathcal{E}_K$ the set of faces e of the element K. Finally, F_{KL}^{n+1} is a numerical flux, which can be decomposed into three parts to have a separate treatment of each mobility term. Namely,

$$F_{KL}^{n+1} = \left(V_{KL}^{n+1} + G_{KL}^{n+1} + C_{KL}^{n+1} \right), \tag{12}$$

where V_{KL}^{n+1}, G_{KL}^{n+1} and C_{KL}^{n+1} are the viscous, buoyancy and capillary numerical fluxes, respectively. In the viscous numerical flux, the mobility is calculated using an upwind method based on the sign of the total velocity, i.e.,

$$V_{KL}^{n+1} = \begin{cases} \Delta t f_w(S_U^{n+1}) u_{T_{KL}} & \text{if } u_{T_{KL}} > 0 \\ \Delta t f_w(S_D^{n+1}) u_{T_{KL}} & \text{otherwise.} \end{cases} \tag{13}$$

Here, S_U and S_D denote the upstream and downstream saturation values, respectively. In the gravity numerical flux, the mobility is computed based on the density differences, i.e.,

$$G_{KL}^{n+1} = \begin{cases} \Delta t T_{KL} f_w(S_U^{n+1}) \lambda_{nw}(S_U^{n+1}) \Delta\rho g(z_L - z_K) & \text{if } \Delta\rho g(z_L - z_K) > 0 \\ \Delta t T_{KL} f_w(S_D^{n+1}) \lambda_{nw}(S_D^{n+1}) \Delta\rho g(z_L - z_K) & \text{otherwise.} \end{cases} \tag{14}$$

Here, $\Delta\rho = (\rho_{nw} - \rho_w)$, and T_{KL} is the interface normalized transmissibility (normalized by the grid cell cross-section area), which is computed as the harmonic average of the neighboring cell parameters, i.e.,

$$T_{KL} = \left(\frac{d_{Ke}}{\mathbf{K}_K} + \frac{d_{eL}}{\mathbf{K}_L} \right)^{-1}, \tag{15}$$

where d_{Ke} and d_{eL} are the distances between the face e_{KL} and the centers of cells K and L, respectively. Finally, the capillary numerical flux is calculated as

$$C_{KL}^{n+1} = \begin{cases} \Delta t T_{KL} f_w(S_U^{n+1}) \lambda_{nw}(S_U^{n+1}) (P_{c_L}^{n+1} - P_{c_K}^{n+1}) & \text{if } u_{T_{KL}} > 0 \\ \Delta t T_{KL} f_w(S_D^{n+1}) \lambda_{nw}(S_D^{n+1}) (P_{c_L}^{n+1} - P_{c_K}^{n+1}) & \text{otherwise.} \end{cases} \tag{16}$$

The quality of the solution of Eq. (10) is highly influenced by the resolution of the spatial and time discretization scheme. The objective of this work is to develop a space-time multilevel adaptive method (ADM-LTS) to solve Eq. (10) accurately and efficiently.

3. ADM-LTS method

In this section, first, the original ADM method [11] is reviewed, then, the newly proposed ADM-LTS algorithm is presented in detail.

3.1. The ADM method

The ADM method is employed to reduce the computational cost associated with the solution of the linear system arising from the linearized problem of Eq. (10).

Let us consider a domain discretized with a high resolution grid which is assumed to be fine enough to capture all relevant physics and to honor the heterogeneous distribution of the geological properties. Given this fine-scale discretization, a hierarchy of n_l nested coarse grids is constructed. Each grid is formed by $N_l = N_{lx} \times N_{ly} \times N_{lz}$ grid cells, where l is the resolution index and $l = 0$ represents the fine grid resolution.

The set of all grid cells belonging to resolution level l is called Π^l. At each time step ADM defines a multilevel grid by combining grid cells belonging to the hierarchy of grids previously defined. Given a multilevel ADM grid, let us define Ω^l as the set of grid cells belonging to all levels from 0 to l which are present in the ADM grid. Additionally, it is convenient to define the set Γ^l as $\Gamma^l = \Omega^l \cap \Pi^l$.

Given an ADM grid formed by the set of grid cells Ω^l, ADM assumes that the fine scale solution can be approximated by employing a sequence of prolongation operators, i.e.

$$\delta \mathsf{x}_f \approx \delta \mathsf{x}' = \hat{\mathsf{P}}_0^1 \dots \hat{\mathsf{P}}_{l-1}^l \delta \mathsf{x}^{ADM}. \tag{17}$$

Here, operator $\hat{\mathsf{P}}_{i-1}^i$ interpolates the solution at level i to the finer resolution level $(i-1)$ and $\delta \mathsf{x}^{ADM}$ is the vector of increment for the ADM solution on the adaptive multilevel grid. The fine-scale Jacobian system is mapped to the ADM grid by

$$\hat{\mathsf{R}}_l^{l-1} \dots \hat{\mathsf{R}}_1^0 \mathsf{J} \hat{\mathsf{P}}_0^1 \dots \hat{\mathsf{P}}_{l-1}^l \delta \mathsf{x}^{ADM} = -\hat{\mathsf{R}}_l^{l-1} \dots \hat{\mathsf{R}}_1^0 \mathsf{r}_f, \tag{18}$$

where $\hat{\mathsf{R}}_i^{i-1}$ is the restriction operator which maps the solution from resolution at level i to coarser level $(i-1)$. In order to ensure mass conservation at all level, a finite volume restriction operator is considered [5]. Thus, the entry (i, j) of a restriction operator reads

$$\hat{\mathsf{R}}_l^{l-1}(i,j) = \begin{cases} 1 & \text{if cell } i \in \Gamma^l \text{ and cell } j \in \Gamma^{l-1}, \\ \delta_{ij} & \text{otherwise.} \end{cases} \tag{19}$$

Additionally, constant interpolation is considered for saturation,

$$\hat{\mathsf{P}}_{l-1}^{l} = \left(\hat{\mathsf{R}}_l^{l-1}\right)^T. \tag{20}$$

Consequently, no solution step is required to compute the prolongation operator.

3.2. ADM method with local time-stepping (ADM-LTS)

At each time step n, having solved the pressure equation and computed the total velocity field, we address the transport equation employing the ADM-LTS algorithm.

First, Eq. (18) is solved with time step Δt over the whole domain on the coarsest grid resolution (l_{max}) formed by cells belonging to $\Pi^{l_{max}}$ and limiting refinement only around the wells. Then, based on the coarse solution obtained, the proper ADM grid resolution is chosen according to a front-tracking criterion. Two alternative front-tracking strategies are considered in this work:

- a criterion based on the saturation difference between neighboring cells. A cell i belonging to level l is refined whenever the saturation difference, as defined in [11], between i and one of its neighbors exceeds a user-defined tolerance ϵ_x.
- a time-dependent criterion combined with the previous one to determine whether cells belonging to Π^0 should stay fine. Let us define $\psi_S = S^{n+1} - S^n$. A fine cell i is kept at the fine resolution only if $\psi_{S_i} > \epsilon_t$, where ϵ_t is a user-defined tolerance. A similar time-based coarsening criterion has successfully been used in the literature for channelized heterogeneous problems where stationary gradients are present [23].

Once the ADM grid resolution has been defined, the solution is recomputed for all cells belonging to $\Omega^{l_{max}-1}$ with a time step $\Delta t_{l_{max}-1} = \Delta t/\eta$ by imposing local boundary conditions as described in detail in the following subsection. Here η is the time refinement ratio. Then, the same operation is repeated for all resolution levels l until $l = 0$ has been reached. Thus, each resolution level l (formed by the set of grid blocks Ω^l) is solved with a time step $\Delta t_l = \Delta t_{l+1}/\eta$. For the finest level ($l = 0$) ADM-LTS only recomputes the solution, with time step $\Delta t_0 = \Delta t/\eta^{l_{max}}$, for a subset, defined Ω_A^0, of the cells belonging to Ω^0. In fact, only fine cells for which $\psi_S = S^{n+\Delta t_1} - S^n > \epsilon_t$ are part of the set Ω_A^0.

The method advances in time for the active cells in Ω_A^0 until they reach $t = t^n + \Delta t_1$. Once they are synchronized, cells in Ω^1 advance in time. At this point, a new set of cells Ω_A^0 is selected and these cells are advanced by Δt_1 performing η Δt_0 time steps. Once all cells in Ω^1 have reached time $t = t^n + \Delta t_2$ another time step Δt_2 can be performed for all cells belonging to Ω^2. This is a recursive procedure which is performed for all levels until all cells have reached time $t^{n+1} = t^n + \Delta t$.

Fig. 1 illustrates a schematic overview of the ADM-LTS method where η and l_{max} are both taken equal to 2. Fig. 2 shows an example of the ADM grid at each step and the refining area. At the global time step Δt, the solution is computed on the coarsest resolution l_{max}. At the intermediate time step the ADM grid resolution is defined and the solution is recomputed with the intermediate time step everywhere except at the coarsest region (middle figure). At the end, the method checks the errors and defines the set of active cells Ω_A^0 (pink region on the right), the solution is recomputed with the smallest time step. Note that the solution at each local time step is performed at a different space-time resolution. Furthermore, all cells belonging to the coarsest level march with the biggest time step size. On the other hand, the saturation at cells in Ω_A^0 (i.e., where higher resolution is needed) naturally advance with smaller time step sizes.

We remark that the quality of the solution and the efficiency of the ADM-LTS algorithm will be significantly affected by the choice of the user-defined tolerances ϵ_x and ϵ_t. Even though, a general strategy cannot be defined, simple analytical solutions (e.g., Buckley-Leverett) can be used to estimate the value of the saturation front and deduce effective values for the tolerances that will have to be determined to obtain the desired trade-off between accuracy and efficiency.

3.2.1. Local systems and local boundary conditions

For each resolution level l, the set of grid cells Ω^l is solved with the corresponding time step $\Delta t_l = \dfrac{\Delta t}{\eta^{(l_{max}-l)}}$. The number of active cells contained by Ω_l is denoted by N_A^l.

When solving for the cells belonging to Ω^l, the numerical flux at the interface between two cells K and L such that $K \in \Omega^l \wedge L \in \Gamma^{l+1}$ is approximated by

$$F_{KL}^{n+\beta(i)} = \frac{F_{KL}^{n+\gamma(j)}}{\eta} \tag{21}$$

where

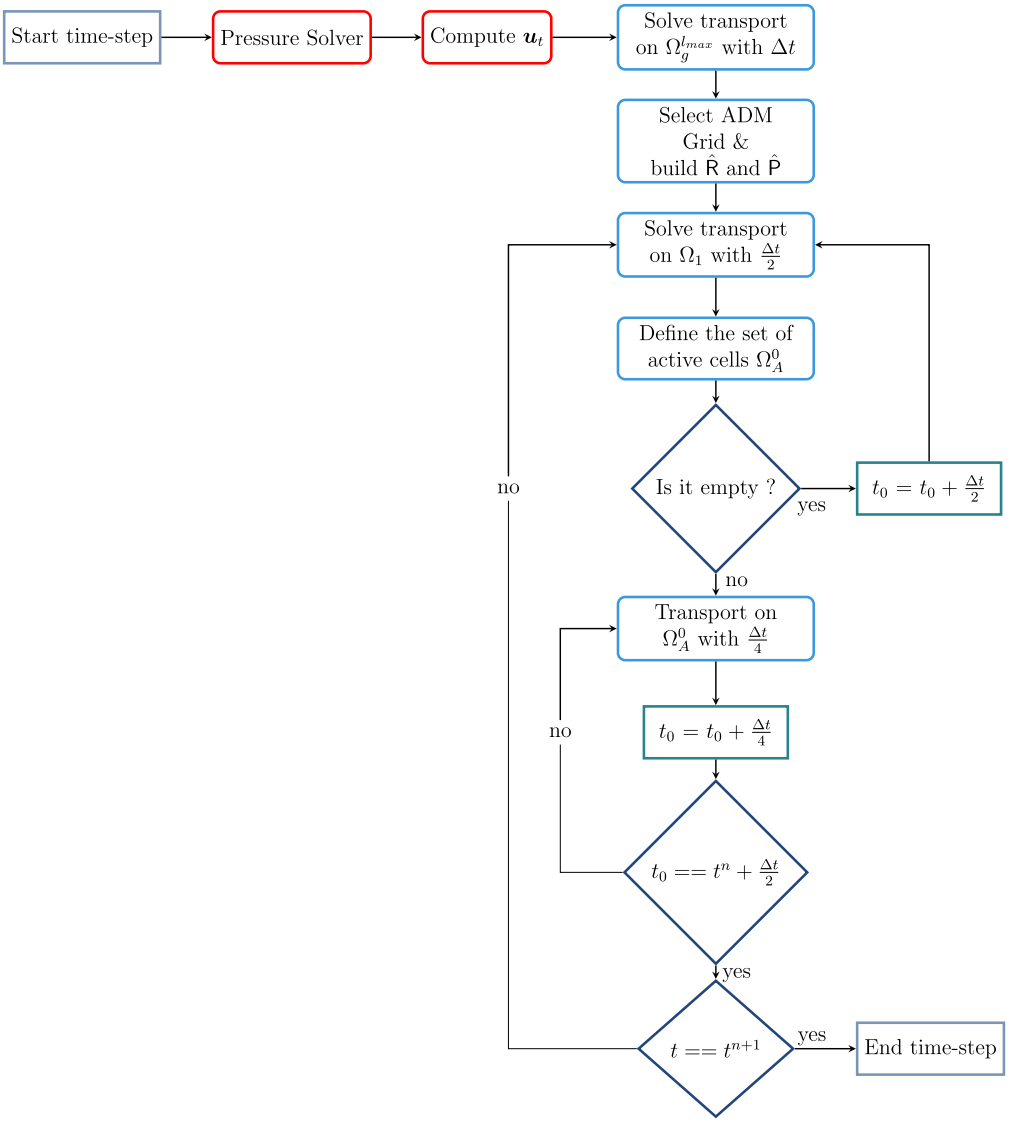

Fig. 1. Schematic overview of a time step for the ADM-LTS strategy with $\eta = 2$ and $l_{max} = 2$.

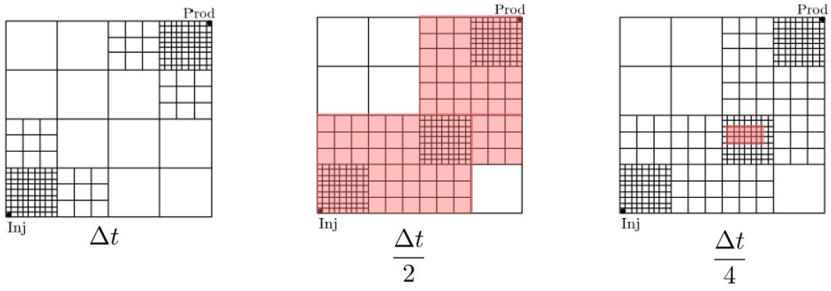

Fig. 2. Example of ADM grid and active regions for the refinement time steps with $\eta = 2$ and $l_{max} = 2$.

$$\beta(i) = \frac{i}{\eta^{(l_{max}-l)}}, \quad i = \{1 \cdots \eta^{(l_{max}-l)}\} \tag{22}$$

$$\gamma(j) = \frac{j}{\eta^{(l_{max}-l-1)}}, \quad j = \{1 \cdots \eta^{(l_{max}-l-1)}\}. \tag{23}$$

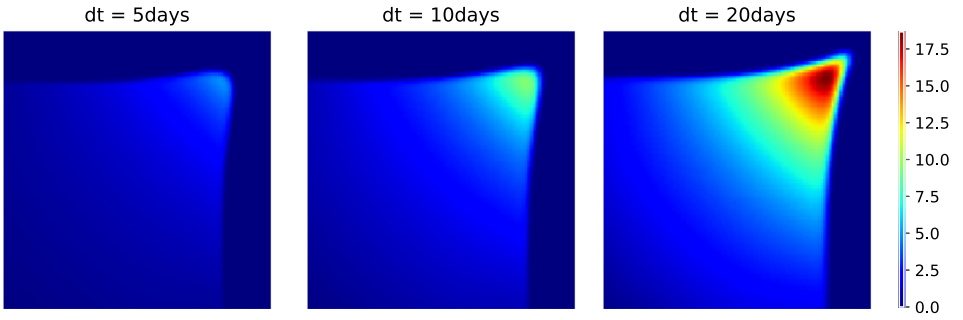

Fig. 3. Test case 1 [99 × 99] - CFL values for different global time steps at time $t = 500$ days.

Thus, Eq. (11) can be modified to account for the presence of different time levels as

$$\begin{aligned} \mathrm{r}_K^{n+\beta(i)} &= \phi(S_K^{n+\beta(i)} - S_K^{n+\beta(i)-1}) \\ &- \frac{1}{|K|}\sum_{e_{KL}\in\mathcal{E}_{KA}} e_{KL} F_{KL}^{n+\beta(i)} - \frac{q_w}{\rho_w}^{n+\beta(i)} - \frac{1}{|K|}\sum_{e_{KL}\in\mathcal{E}_{KL}} e_{KL}\frac{F_{KL}^{n+\gamma(j)}}{\eta}. \end{aligned} \tag{24}$$

Here, $\mathcal{E}_{KA}$ is the set of interface fluxes exchanged between two cells K and L both belonging to Ω^l. Additionally, $\mathcal{E}_{KL}$ is the set of fluxes at the interface between two cells K and L where $K \in \Omega^l$ and $L \in \Gamma^{l+1}$. Note that, for $l = 0$ the residual for the active cells is the same described in Eq. (11), but $\mathcal{E}_{KL}$ would be the set of fluxes at the interface between Ω_A^0 and $\Omega^1 \setminus \Omega_A^0$.

We remark that, for each level l, the linear system to be solved has size $N_A^l \times N_A^l$, which is significantly smaller than the full fine-scale system. At each time step, only a sub-set of the cells of each level l is restricted and prolonged.

The following section presents a study of the performance of the ADM-LTS method for various 2D and 3D test cases involving different fluid physics.

4. Numerical results

The performance of the newly developed ADM-LTS strategy is thoroughly investigated for several challenging test cases. For all the cases presented, quadratic relative permeability curves are considered. Gravitational and capillary forces are only considered in test cases 2 and 7, respectively. Furthermore, all errors are computed with respect to a reference solution, obtained by employing a high resolution discretization both in space and in time.

4.1. Test case 1: 2D homogeneous reservoir

The first test case is a 100×100 [m^2] homogeneous reservoir, with isotropic permeability of 5×10^{-15} [m^2]. A pressure-constrained wetting-phase injector well is positioned in the bottom-left corner of the domain with a pressure $p_{inj} = 10^8$ [Pa], whereas a production well is present in the top-right corner with a relative pressure of $p_{prod} = 0$ [Pa]. The phase viscosity values are $\mu_w = 10^{-3}$ [Pa · s] and $\mu_{nw} = 10^{-2}$ [Pa · s] for the wetting and non wetting phase, respectively. The final simulated time is 600 [days] after injection has started.

A fine-scale grid with 99×99 cells is imposed on the domain. ADM-LTS employs, a time refining ratio $\eta = 2$ and a space coarsening ratio equal to 3 in all directions. The user-defined tolerances for the coarsening and refinement criteria are $\epsilon_x = 0.07$ and $\epsilon_t = 5 \times 10^{-2}$.

Simulations are run employing three different global time step sizes: 5, 10 and 20 days. Fig. 3 reports the CFL values at time $t = 500$ days for the three different time steps for fine-scale in space simulations.

Fig. 4 shows a comparison of the ADM-LTS solution with the reference solution (on the left) at time $t = 500$ [days] using three different sizes of the global time steps.

Fig. 5 reports the error for the saturation at time $t = 500$ days between a reference solution and the ADM method with fine time steps (first column) with the LTS approach (second column) and with the coarse time steps (third column) for the three different time steps sizes $\Delta t = 5$ (first row), $\Delta t = 10$ (second row) and $\Delta t = 20$ (third row). In all cases the AMD-LTS approach improves the errors with respect to the coarse time step approach.

The complexity of the algorithm is shown in Fig. 6. In particular, each column represents the total amount of active cells multiplied by the number of Newton iterations involved to compute the solution, for the three approaches and for the three different global time step sizes. Note that, to obtain the solution at time $t = 600$ [days], 120, 60 and 30 global time steps have been performed using the three analyzed time steps. We remark that the errors obtained by employing the original ADM method with a fine time step are comparable to those obtained with ADM-LTS in terms of accuracy.

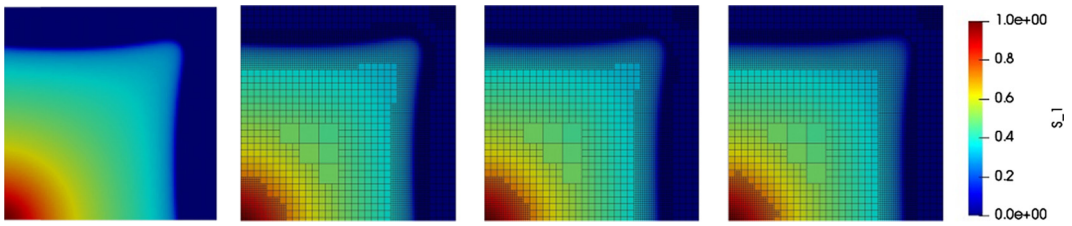

Fig. 4. Test case 1 [99×99] - Reference solution (first column) and ADM-LTS solution using a global time step size: $\Delta t = 5, 10$ and 20 [days] at time $t = 500$ days for the second, third and fourth column, respectively.

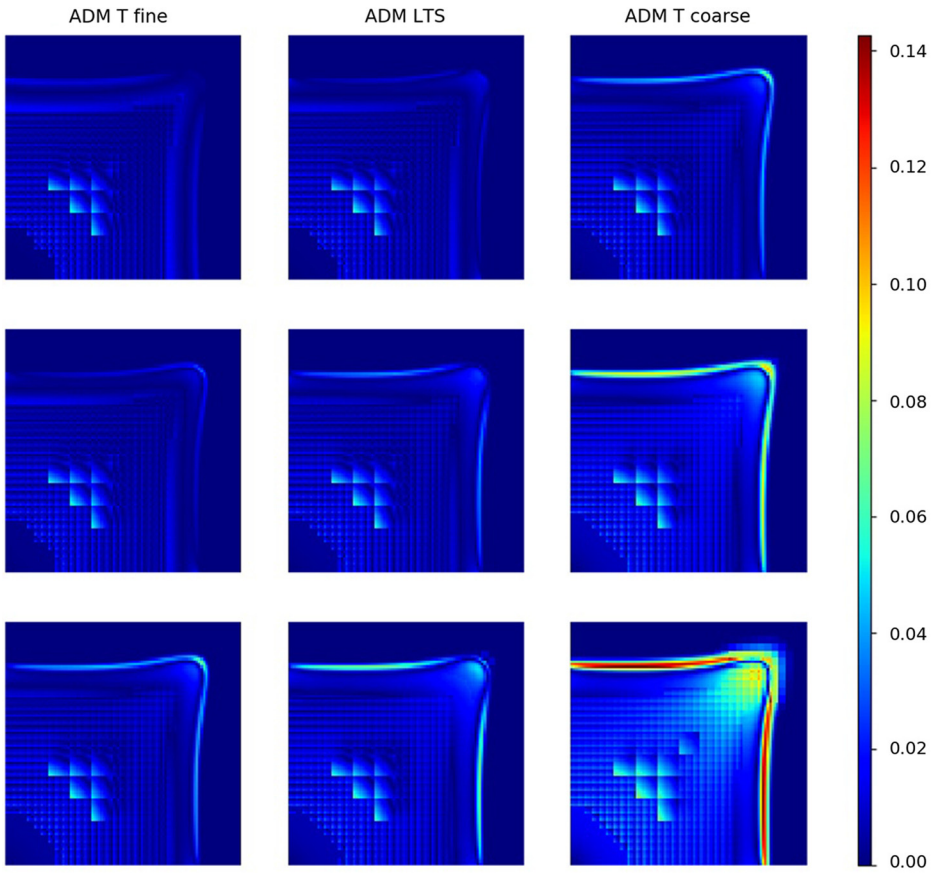

Fig. 5. Test case 1 [99×99] - Saturation errors for the ADM method with fine time steps (first column), ADM-LTS method (second column) and ADM coarse time steps method (third column) for the three different global time step sizes.

Fig. 7 shows the complexity of a single global time step. For the ADM method with fine time steps, the local steps are just the small steps applied at the whole domain. At the end of the local steps both the ADM-LTS method and the ADM fine step method reach the same time. For the ADM-LTS method, local step 1 indicates the global step on the coarsest grid, step 2 and 5 are the intermediate time steps performed on level 0 and 1 of the ADM grid, and the other local steps are the small time steps for the active cells detected by the error estimator in time. In particular, we can notice that the intermediate time steps have almost the same complexity of the small time steps of the ADM fine method, even if the size of the time step is two times bigger with almost the same number of active cells. This is due to the improvement of the initial guess for the Newton loop. In the intermediate time steps we use as initial guess a linear combination of the solution of the previous time t^n and the solution obtained on the coarsest grid at the new global time t^{n+1}. In the small time steps is not necessary to perform this technique since a small step is used to advance in time.

The same test case is analyzed after performing a 2×2 refinement of the space fine-scale grid. In order to obtain a reasonable solution, using a global Δt equal to 20 [days], we need to compute more local time steps inside the global one, so a refining ratio equal to 4 has been taken into account.

Fig. 8 reports the complexity for the entire simulation using ADM-LTS method and the ADM with fine time steps. To obtain the solution at final time $t = 600$ [days] with a global time step equal to 20 days, the same number of global time

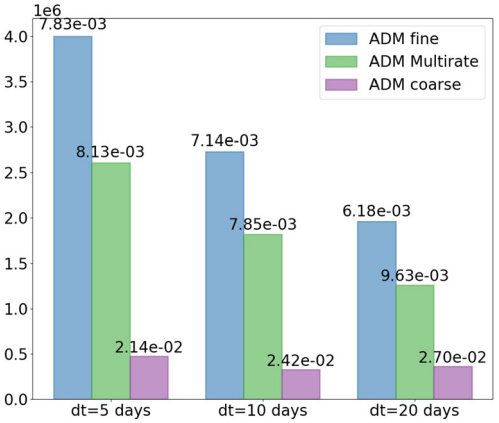

Fig. 6. Test case 1 [99 × 99] - Total amount of active cells multiplied by number of Newton iterations for the three different time step sizes. On the top of each bar the mean in time of the averaged absolute difference respect to the reference solution for the saturation is displayed $E_s = \text{mean}|S(t_f) - S_{ref}(t_f)|$ where t_f is the final time 600 days.

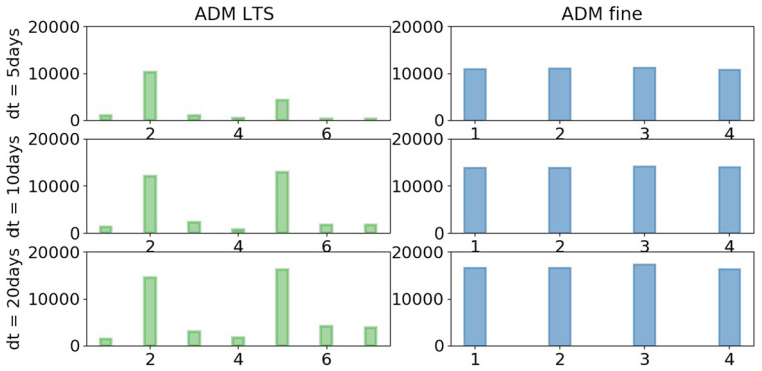

Fig. 7. Test case 1 [99 × 99] - Computational complexity history at each local times step within a global step. The computation complexity is the number of active cells multiplied by the number of Newton iterations.

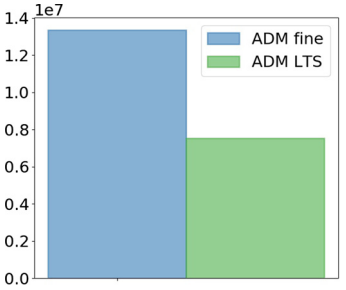

Fig. 8. Test case 1 [198 × 198] - Total amount of active cells multiplied by number of Newton iterations for the ADM with fine time steps and the ADM LTS method.

step are involved (30 time steps in total). Of course the number of local time step for both the LTS method and the fine time steps approach has increased; but the ratio between active cells and total cells decreases.

Fig. 9 shows the averaged number of active cells times the number of Newton iterations for each local time step within a global time step.

In Fig. 10 we can see that the ADM-LTS approach reduces the errors obtained using a coarse grid in time.

4.2. Test case 2: 3D homogeneous reservoir

A 3D 108 × 108 × 108 [m^3] homogeneous reservoir is considered in this test case. The domain is discretized, at the fine-scale, with a 54 × 54 × 54 Cartesian grid for a total of 157464 cells. The physical parameters are the same of the first

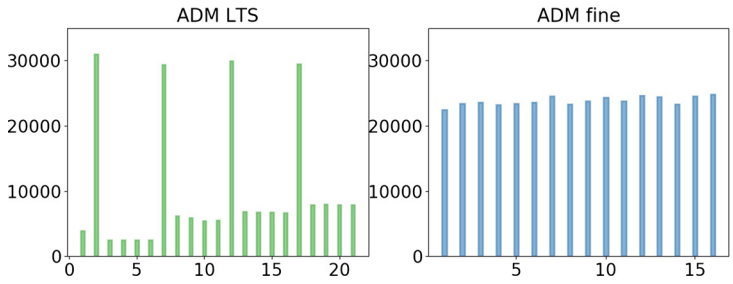

Fig. 9. Test case 1 [198 × 198] - Computational complexity history at each local times step within a global step. The computation complexity is the number of active cells multiplied by the number of Newton iterations.

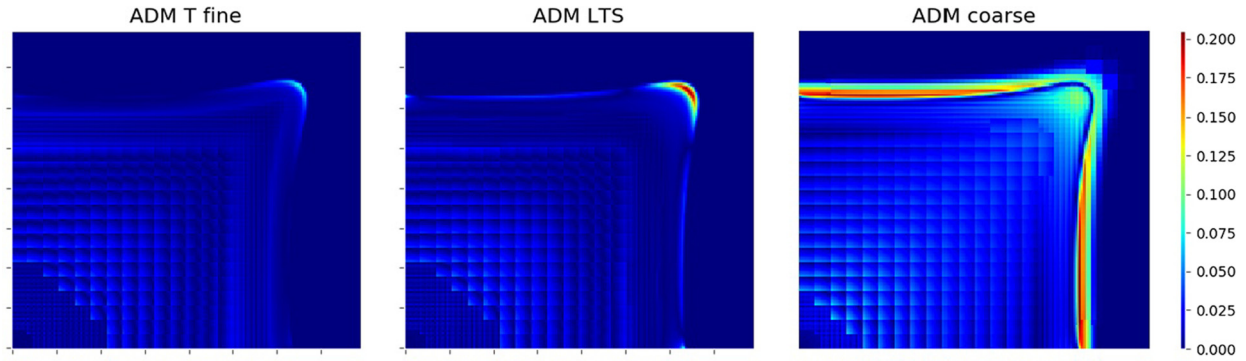

Fig. 10. Test case 1 [198 × 198] - Saturation errors at time $t = 540$ [days] for the ADM method with fine grid in time (left), ADM-LTS method (center) and the ADM method with coarse grid in time (right).

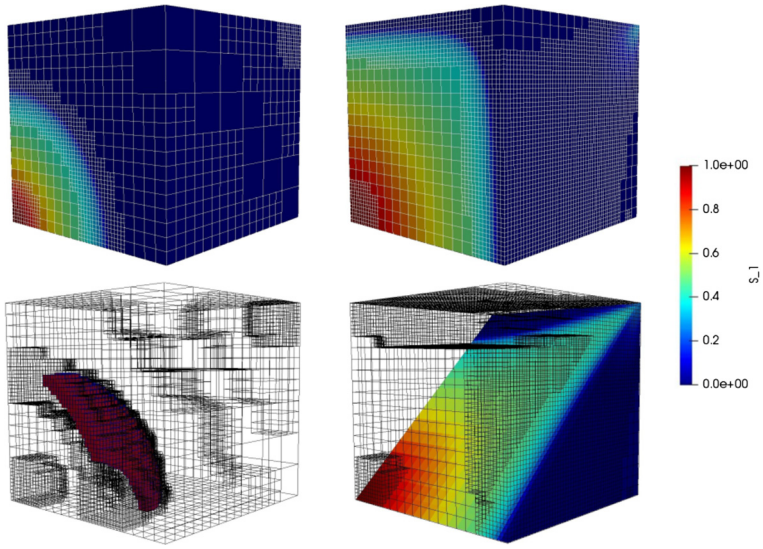

Fig. 11. Test case 2 - Saturation profile (top row) at time $t = 1500$ days (left) and at time $t = 8750$ days (right) for the case without gravity. Active cells for the level $l_{ref=0}$ at time $t = 1500$ (bottom-left) and saturation profile inside the domain at time $t = 8750$ (bottom-right).

test case. The size of the global steps is equal to 125 days. The simulation ends after 70 global steps. The tolerances for the coarsening criteria in space and time are set to be $\epsilon_x = 0.2$ and $\epsilon_t = 5 \times 10^{-2}$.

Fig. 11 reports the saturation maps at two different simulation times (on the top) neglecting the gravity effects. It also displays the set of active cells Ω_A^0 at time $t = 1500$ days (left, bottom) and a section of the solution at final time $t = 8750$ days (right, bottom). Note that ADM-LTS automatically employs fine cells only around the advancing saturation front and that the active cells in time are only a fraction of them.

Fig. 12 shows the saturation maps and the active cells Ω_A^0 at different times considering the same scenario but introducing a density ratio of $\rho_w/\rho_{nw} = 5/4$. As expected, the heavier fluid occupies the bottom of the reservoir.

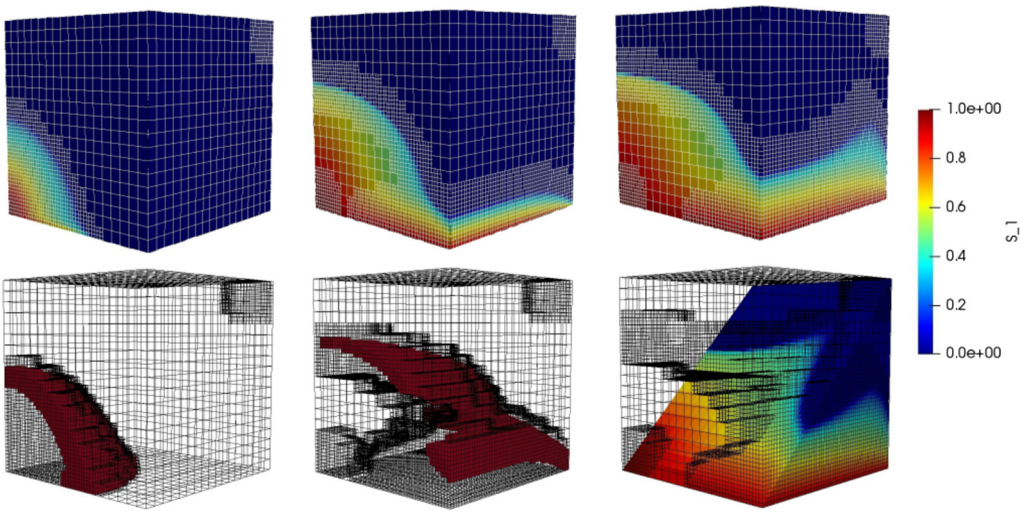

Fig. 12. Test case 2 - Saturation profile (top row) at time $t = 1500$ days (left), $t = 6375$ (center) and $t = 8750$ days (right) for the case with gravity. Active cells for the level $l_{ref=0}$ at time $t = 1500$ (bottom-left), active cells for the level $l_{ref=0}$ at time $t = 6375$ (bottom-center) and saturation profile inside the domain at time $t = 8750$ (bottom-right).

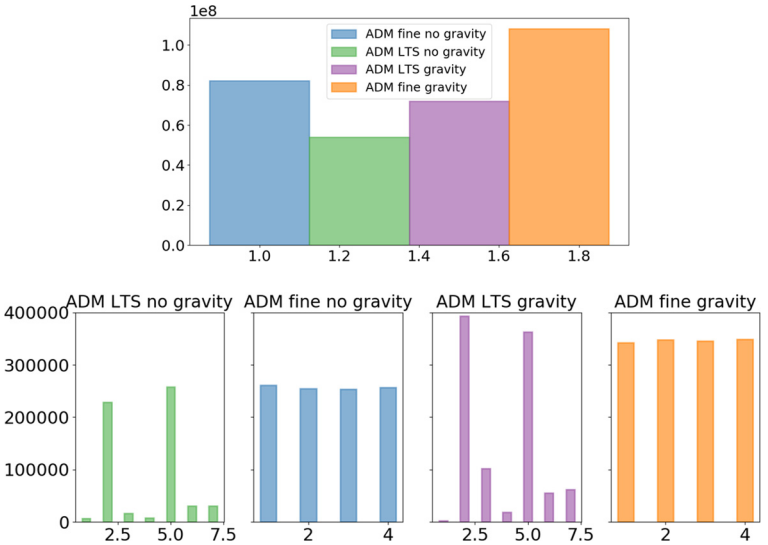

Fig. 13. Test case 2 - Computational complexity – total amount of active cells multiplied by the count of Newton iterations for different scenarios (top). Computational complexity history for ADM-LTS and ADM fine-scale time are also presented (bottom).

Fig. 13 shows the total and the mean computational complexity per local time step for both ADM-LTS and ADM methods. This figure illustrates the results with fine time steps, with and without gravity effects. The transport equation, in the presence of gravitational forces, becomes highly nonlinear. As a consequence, more Newton iterations are required to converge compared with the case without gravitational effects. Note that, as shown in Fig. 14, the number of ADM-LTS active cells for the two different scenarios is the same during the entire simulation. The number of active cells increases during the progress of the simulation time, resulting in reduction of the relative errors (Fig. 14). The errors of ADM-LTS for the cases with and without gravity are comparable.

4.3. Test case 3: 2D homogeneous reservoir with barrier

A 2D homogeneous reservoir with low permeability barriers is considered, as shown in Fig. 15. The same permeability field was presented in [23]. The domain dimensions and the physical parameters are the same of the first test case, the same 99×99 fine scale grid is imposed. The global time step is equal to 50 [days] and the simulation ends after 100 global time steps ($t = 5000$ days).

Simulations are carried out both with the original ADM method employing a global fine time-step and with ADM-LTS. The coarsening and the time-refinement criteria tolerances are set to $\epsilon_x = 0.05$ and $\epsilon_t = 0.005$.

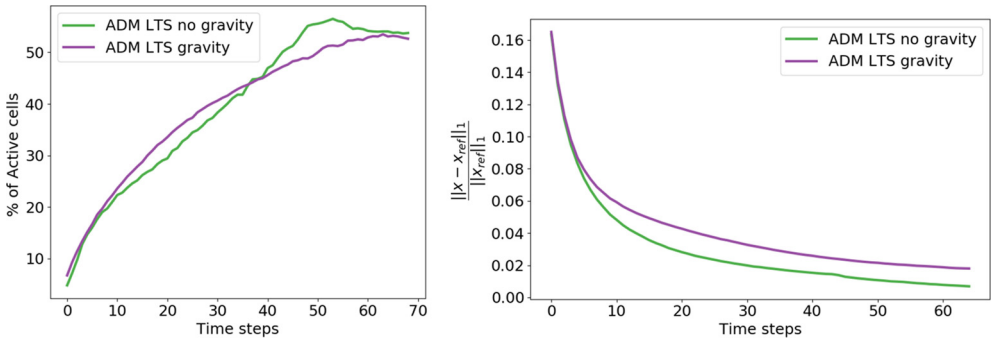

Fig. 14. Test case 2 - Number of ADM-LTS active cells for the test cases with and without gravity (left). Also shown (right) are the saturation l^1-norm errors.

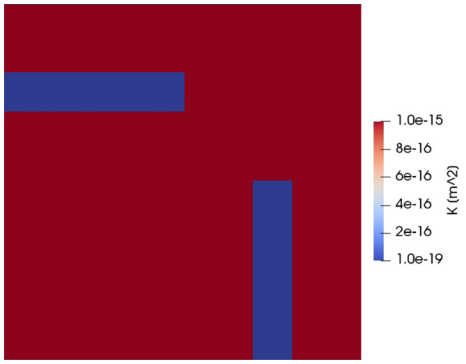

Fig. 15. Test case 3 - Absolute permeability field.

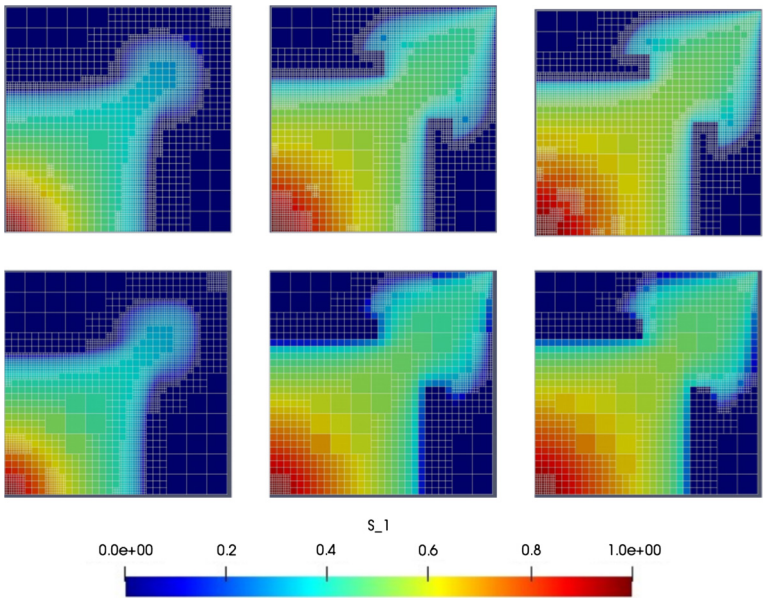

Fig. 16. Test case 3 - Saturation profile and ADM grid at different time steps (columns) for ADM with coarse time steps and classical ADM grid resolution (first row) and for ADM-LTS method with the new ADM grid resolution (second row).

Fig. 16 shows a comparison of the saturation profile and the grid resolution for the two different strategies. The original ADM method with a saturation difference-based coarsening criterion (top row) employs a large number of fine grid cells wherever saturation gradients are present even if they are stationary. On the other hand the newly proposed grid resolution criterion (bottom row) for the ADM-LTS approach uses fine cells only in those regions where the saturation gradient is moving, reducing the number of active cells.

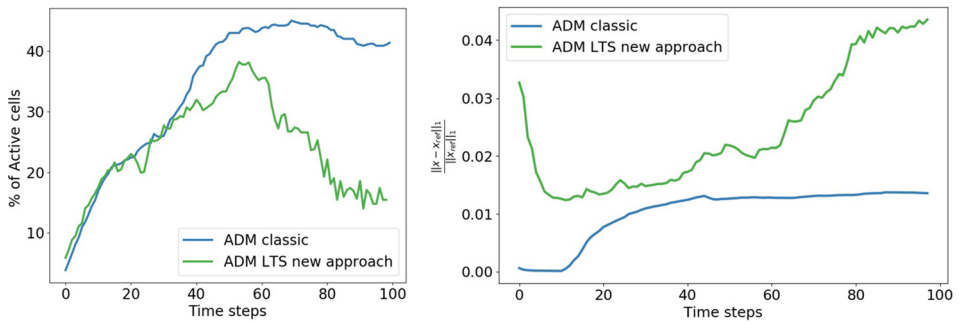

Fig. 17. Test case 3 - number of active cells employed in ADM with fine grid in time and ADM-LTS simulations expressed as percentage of fine grid cells (left) and the saturation relative errors in l^1-norm for the ADM fine and ADM-LTS method (right).

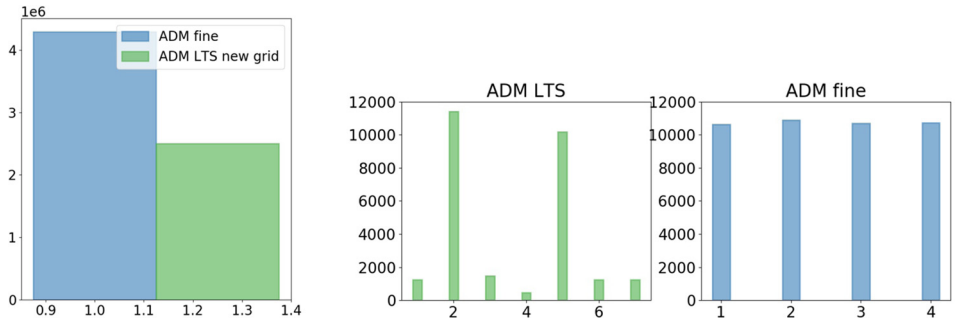

Fig. 18. Test case 3 - Total amount of active cells multiplied by number of Newton iterations (left) and computational complexity history at each local times step within a global step (right) for the ADM with fine time steps approach and for the ADM-LTS method.

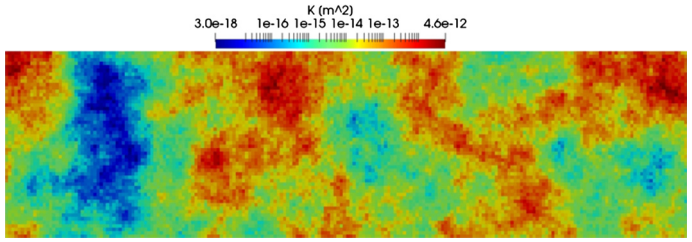

Fig. 19. Test case 4 - Natural logarithm of the permeability.

Fig. 17 reports the evolution of the active grid cells percentage for the two different approaches (left) and the evolution of the relative saturation error in l^1-norm (right). In the early steps, we can see that the ADM fine with just the gradient in space criterion approach employs almost the same number of active grid cells used by the ADM-LTS method. For the ADM with fine time steps at every small local time step we solve both the flow and the transport equations, instead for the ADM-LTS approach only the transport equation is solved for the local steps. This is the reason why in the first five steps the saturation errors for the ADM-LTS approach are larger with respect to the ADM fine steps approach. Instead, in the last steps the errors increase because a lower number of fine grid cells has been used.

Fig. 18 shows the total complexity (number of active cells multiplied by the number of Newton iterations) for the ADM with fine steps and the ADM-LTS approach. Note that the local time steps of ADM-LTS method reduce the complexity of the system compared to the classical ADM approach.

4.4. Test case 4: heterogeneous reservoir (SPE10 top layer)

In this test case a heterogeneous reservoir is considered. The permeability map is the top layer of the SPE10 test case [24] and it is presented, in logarithmic scale, in Fig. 19. The size of the reservoir is 2200×600 [m^2] and a 216×54 grid is employed at the finest level. The injector is at the top left corner and has a constrained pressure 10^7 [Pa]. A producer is, instead, located at the bottom right corner of the domain with a pressure equal to 0 [Pa]. The porosity of the reservoir ϕ is equal to 0.2. The viscosity for the wetting phase is 10^{-5} [Pa $\cdot$ s], whereas, for the non-wetting phase, is 10^{-4} [Pa $\cdot$ s]. The coarsening ratio for the space grid is equal to 2 as well as the time refining ratio. The error tolerance for the time estimator is equal to 5×10^{-2}.

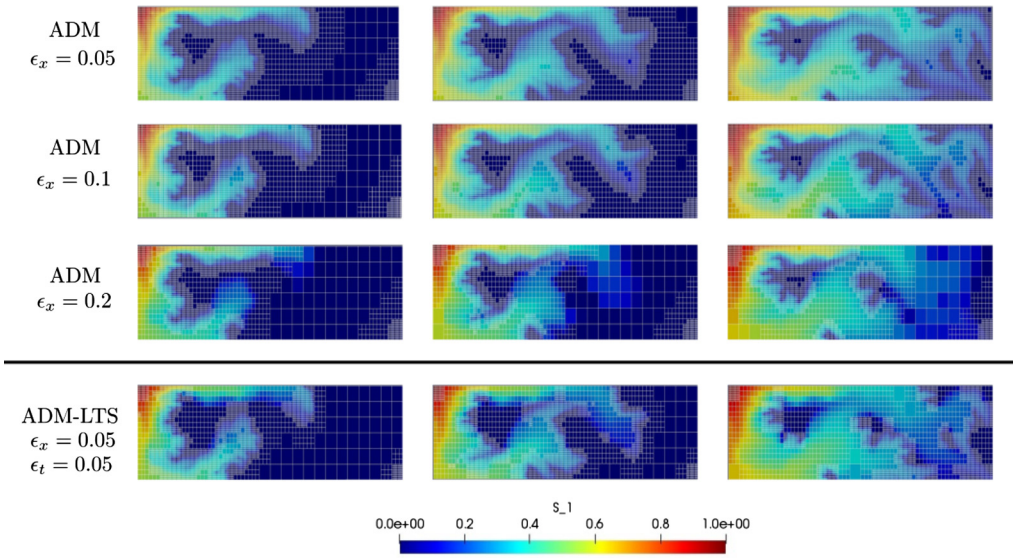

Fig. 20. Test case 4 - Saturation map and ADM grid for the ADM with fine time step approach with classical grid criterion for different values of the threshold $\epsilon_x = 0.05, 0.1, 0.2$ (row 1, 2, and 3) and for the ADM-LTS method with the new grid criterion $\epsilon_x = 0.05$ and $\epsilon_t = 0.05$ (row 4) at time $t = 1200$ days (first column), $t = 15000$ days (second column) and $t = 20000$ days (third column).

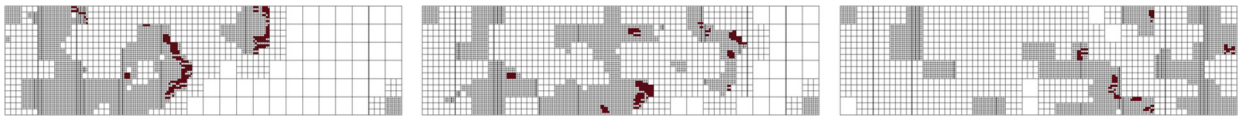

Fig. 21. Test case 4 - Active cells for the refinement in time, at time $t = 1200$ days (left), $t = 15000$ days (center) and $t = 20000$ days (right).

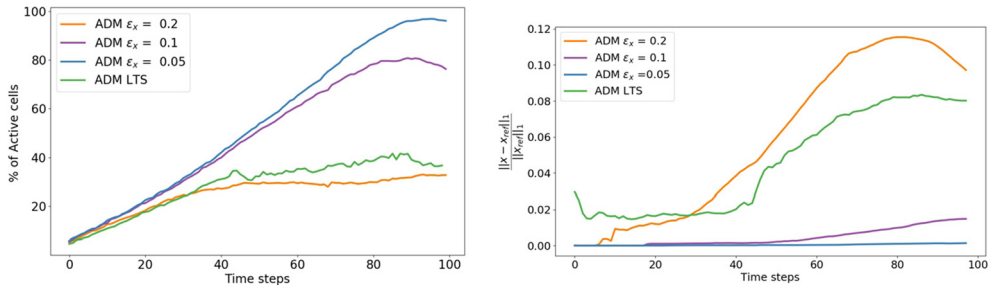

Fig. 22. Test case 4 - Number of active cells expressed as percentage of fine grid cells (left) and saturation relative errors in l^1-norm (right) for the ADM with fine grid in time with different values of the threshold and for the ADM-LTS simulation.

Fig. 20 reports the saturation map and the ADM grid for different threshold values of the ADM grid resolution criterion using the classical ADM approach with fine time steps, and the ADM-LTS approach with the new grid resolution strategy. The classical approach uses, for small threshold values, a large number of fine grid cells. If we relax the threshold parameter the method is not able to capture the fronts. Thanks to the new ADM-LTS approach, the method is able to apply the fine grid cells only where the front is moving fast (high permeability regions).

Fig. 21 shows the active cells in time at the finest level $l_{ref} = 2$ for different global time steps. The method recomputes the solution with small time steps only for a few percentage of cells where the front crosses high permeability regions. In fact, in the last snapshot, the saturation profile is almost developed everywhere and so, the set of active cells is very small.

In Fig. 22 we compare the number of active cells and the saturation errors for the different simulations. Using the classical ADM approach with small values of the tolerance a lot of active grid cells are employed giving very small errors. The classical ADM approach with larger tolerance value and the ADM-LTS method are comparable in terms of active cells during all the simulation but the ADM-LTS approach gives better results in term of errors.

Fig. 23 reports the complexity of the four simulations. The ADM approach with fine grid in time and small threshold values is really expensive. The ADM-LTS approach is comparable to the ADM with fine time step approach and large value of ϵ_x but, as shown previously, the solution of the classic ADM, in this case, is not as accurate.

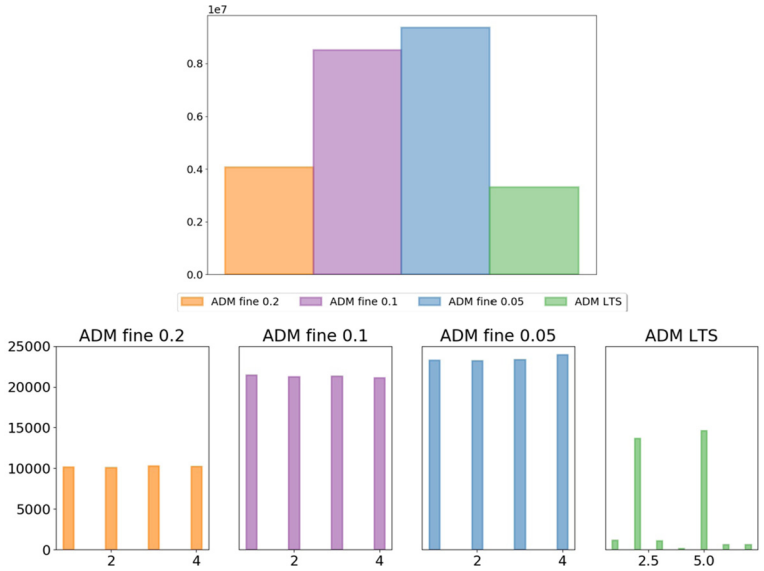

Fig. 23. Test case 4 - Total amount of active cells multiplied by number of Newton iterations (top) and computational complexity history at each local times step within a global step (bottom) for the ADM approach.

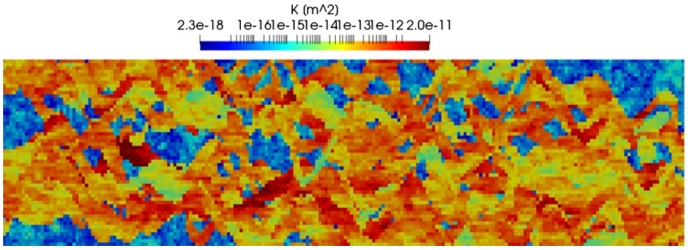

Fig. 24. Test case 5 - Natural logarithm of the permeability.

4.5. Test case 5: heterogeneous reservoir (SPE10 bottom layer)

The permeability of SPE10 bottom layer is used for this test case, as shown in Fig. 24. This layer, with respect to the previous case has higher contrasts and more a channelized distribution.

The global time step is equal to 10 days and the simulation ends after 50 global time steps. The input parameters for the wells and the physical properties are identical to Test Case 4.

The top 2 rows of Fig. 25 show the saturation distribution at simulation time of 150, 250 and 350 days obtained with $\epsilon_x = 0.15$ and $\epsilon_x = 0.2$, respectively. The bottom rows, instead, show the saturation map, at the same simulations times, obtained by employing the ADM-LTS method with $\epsilon_x = 0.05$ and $\epsilon_t = 5 \times 10^{-2}$ and $\epsilon_t = 5 \times 10^{-3}$. The classic ADM approach employs a large number of active cell during the simulation, instead the ADM-LTS method is able to select a fine scale grid only where the fronts are moving.

Fig. 26 shows the active cells in time for $l_{ref} = 2$ at time 150, 250 and 350 days. As expected, for smaller value of the threshold more cells are involved in the refinement step.

The history of the percentage of active cells employed by the different simulation strategies for the various tolerances is shown in Fig. 27 (left), along with the l^1 norm of the saturation error (right). For both the ADM-LTS tolerance values less active cells are involved respect to the classical ADM approach. Since a smaller number of cells is employed, the saturation errors are higher but still of the same order of magnitude.

Fig. 28 reports the complexity of the four simulations for different tolerance values.

4.6. Test case 6: heterogeneous reservoirs with different layering orientations

A 500×500 m^2 2D reservoir is considered on which a 99×99 grid is imposed. The fluid properties, the location of the wells and their constraints are the same as in the previous test cases. Five sets of permeability fields, with different layering orientation and created using sequential Gaussian simulations with spherical variogram and dimensionless correlation lengths 0.5 and 0.02 as proposed in [25], are considered. Each set consists of 20 statistically identical realizations.

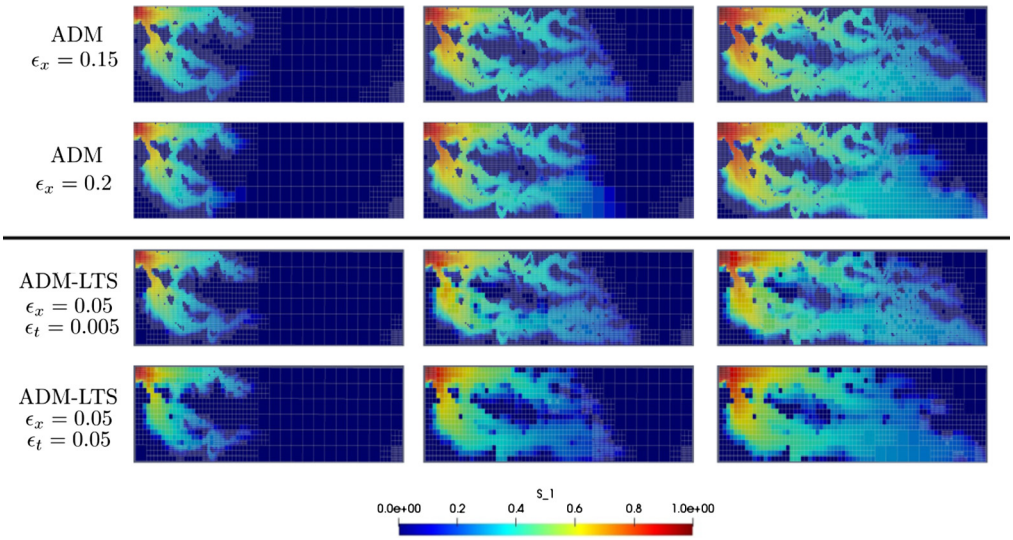

Fig. 25. Test case 5 - Saturation map and ADM grid at 150, 250 and 350 days for the ADM approach with fine time steps and the ADM-LTS approach.

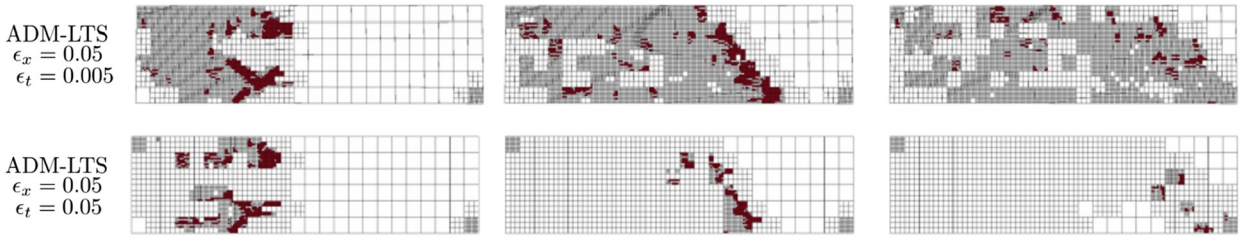

Fig. 26. Test case 5 - Active cells for the refinement level $l_{ref} = 2$, at 150 (left), 250 (center) and 350 (right) days for the two threshold values.

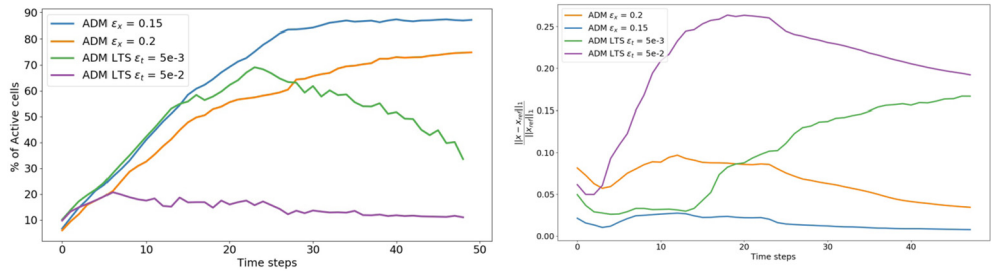

Fig. 27. Test case 5 - Number of active cells expressed as percentage of fine grid cells (left) and saturation relative errors in l^1-norm (right) for the ADM with fine grid in time and for the ADM-LTS simulations.

Fig. 29 shows one realization for each set. Injection of the wetting phase, for 560 days, is simulated for each realization. Simulations are run with the ADM-LTS method. For all runs, the spatial coarsening criterion tolerance is $\epsilon_x = 0.008$. Two different values are instead considered for the time-based criterion tolerance, ϵ_t: 5×10^{-2} and 5×10^{-3}.

Fig. 30 shows a comparison, for one permeability realization of each set, of the saturation map at the end of the simulation obtained with fine-scale (time and space) simulation (top row), ADM-LTS employing a fixed refined time-step.

Fig. 31 displays the active cells in time for the last refinement level of the last global time step. As expected, using a bigger value of the tolerance for the time error estimator, just few cells need to be computed with small time steps. Moreover, the space grid changes and allows to use coarser grid cells.

Fig. 32 represents the mean and the standard deviations of the complexity for the ADM-LTS method using the two different time-based criterion tolerances and for the solution computed with the fine grid resolution both in space and in time. Note that the y-axis scale for the two pictures are different.

Fig. 33 shows the mean and the standard deviations of the saturation errors respect to the reference solution for the ADM-LTS method using the two different time-based criterion tolerances. From these studies, one can conclude that the ADM-LTS performs robustly when several equiprobable realizations are considered. In other words, the error and computational complexities for all 20 realizations are not much different compared with the average values.

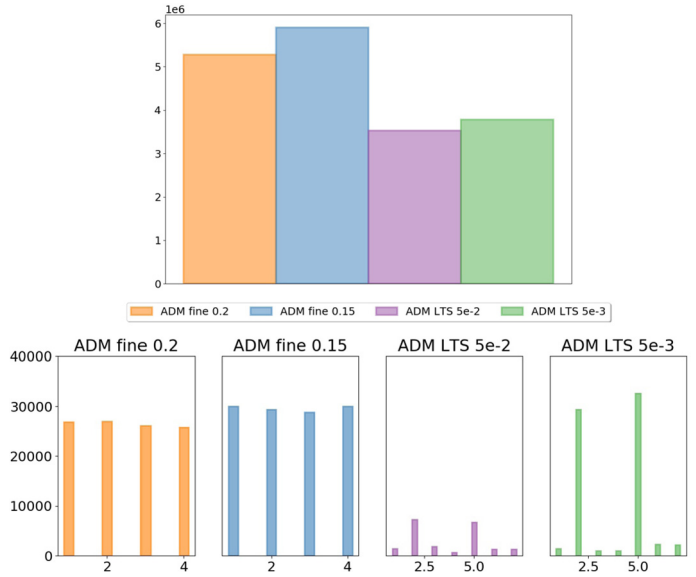

Fig. 28. Test case 5 - Total amount of active cells multiplied by number of Newton iterations (top) and computational complexity history at each local times step within a global step (bottom) for the ADM approach.

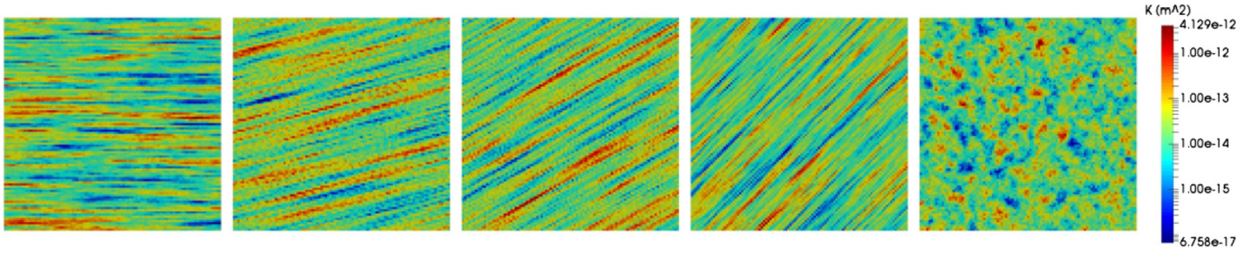

Fig. 29. Test case 6 - One of the 20 realization of each of the 5 sets of permeability fields with different angles (0 deg, 15 deg, 30 deg, 45 deg and patchy from left to right).

Table 1
Test case 7 - Wells coordinates and constraints.

Well	x	y	Pressure [bar]
Prod (W1)	1	1	120
Prod (W2)	99	1	120
Prod (W3)	99	99	100
Prod (W4)	1	99	100
Inj (W5)	50	50	150

4.7. Test case 7: capillary forces

A 500×500 [m^2] heterogeneous reservoir is considered. The fine-scale grid contains 99×99 cells. The phase viscosity values are $\mu_w = 1e-4$ [Pa $\cdot$ s] and $\mu_{nw} = 1e-3$ [Pa $\cdot$ s]. Five pressure-constrained wells are present, as shown in Fig. 34 along with the heterogeneous permeability field. The well locations and the pressure values are presented in Table 1.

The simulation is run until 2500 [days] after injection is reached. A time step size equal to 10 [days] is used. The ADM-LTS employs a time refining ratio of $\eta = 2$ and a space coarsening ratio of 3. The user-defined tolerances are set as $\epsilon_x = 0.25$ and $\epsilon_t = 1 \times 10^{-2}$. The same capillary pressure function as in [12,26] is considered, i.e.,

$$P_c = \sigma \cos(\theta) \sqrt{\frac{\phi}{K}} J(S), \tag{25}$$

where

$$J(S) = 0.05 \left(\frac{1}{S} \right)^{-0.5}. \tag{26}$$

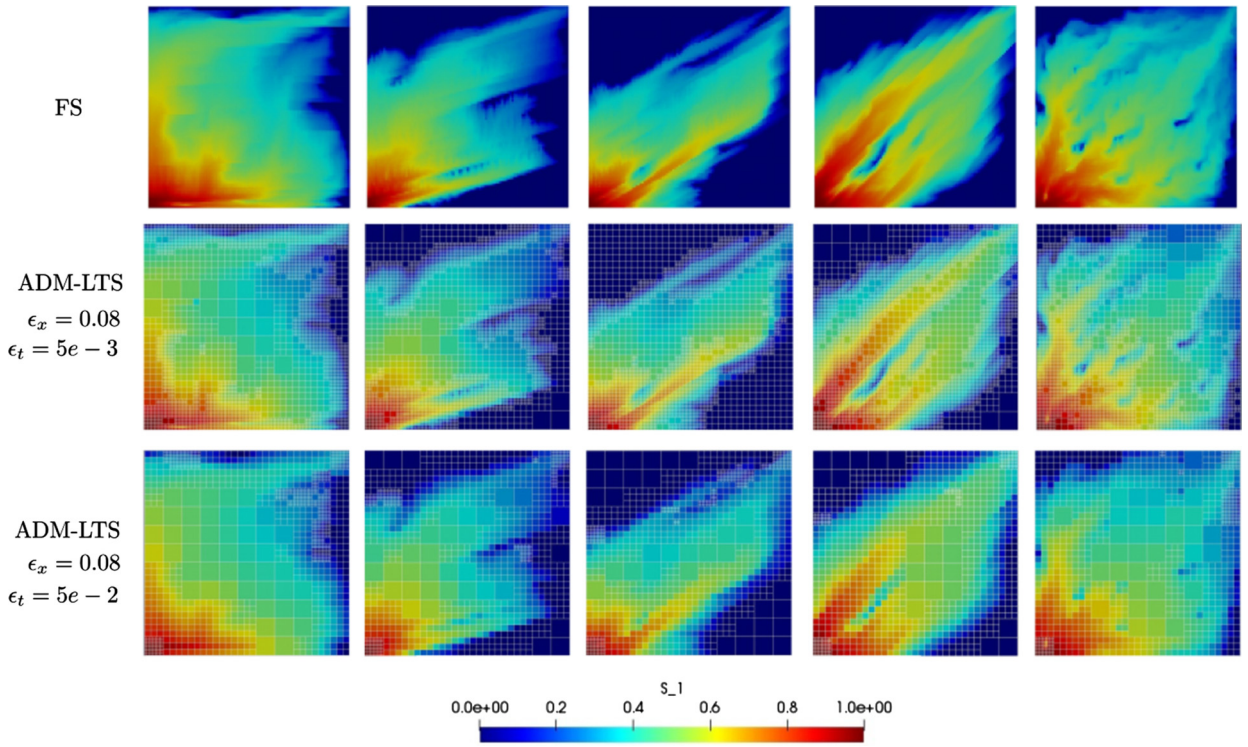

Fig. 30. Test case 6 - Comparison of the saturation profile, for one realization of each set of permeability fields at time $t = 560$ days. Two different threshold values for the time error estimator are employed for the ADM-LTS simulation (center row and bottom row), the fine scale solution are also shown (top row).

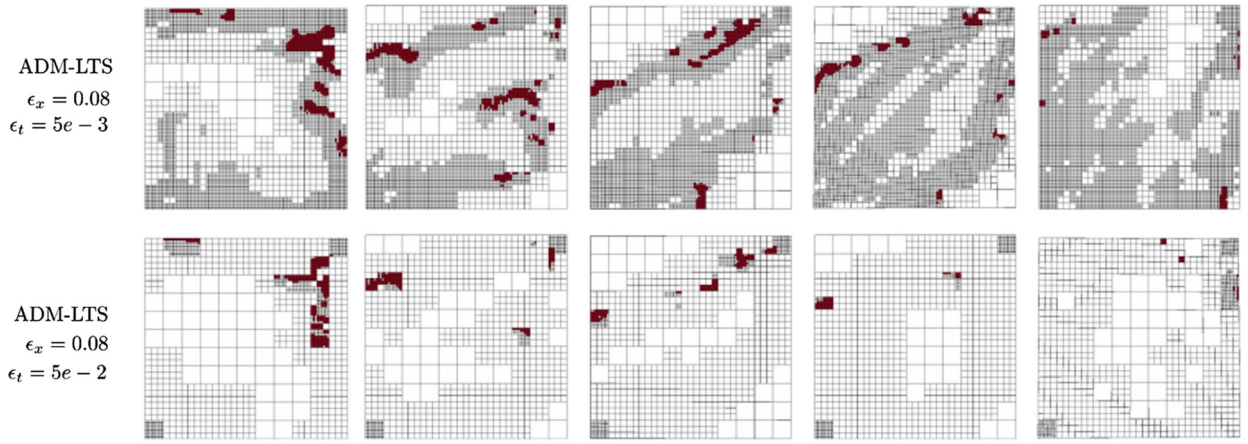

Fig. 31. Test case 6 - Active calls at the last refinement level for the last global time step using two different threshold values for the error estimator in time.

Here, S is the saturation of the wetting phase, $\sigma = 4.361 \times 10^{-2}$ [Pa · m] the surface tension and $\theta = 0$ the contact angle. Fig. 35 compares the reference solution (fine-scale) and the ADM-LTS approach with and without including the effect of capillary pressure. The ADM-LTS approach, as shown in Fig. 36, in presence of capillary pressure employs more active cells, since the saturation map is more complex compared with the case without capillary effects. In this test case, the complex physics induced by capillary heterogeneity is present in almost the entire computational domain. Therefore, the advancing saturation front is present in a large sub-region of the domain. As the result, in this case, 70% of the active cells are used to obtain accurate solutions. Fig. 36 shows the errors in l^1 norm for the ADM-LTS method with and without capillary effects. After the global time step 150, the saturation error increases due to coarsening some fine cells. Then after 200 days, the error is stabilized.

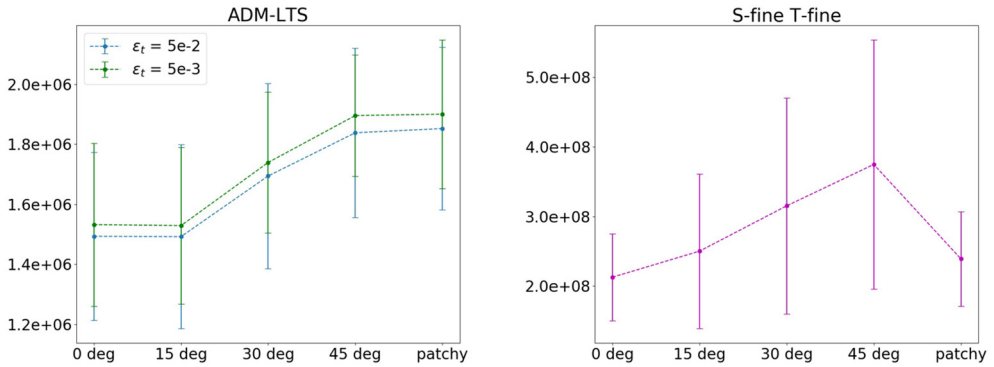

Fig. 32. Test case 6 - Mean and standard deviation of complexity over 20 realization for the ADM-LTS method (left) and for the reference solution computed with fine grid resolution both in space and time (right).

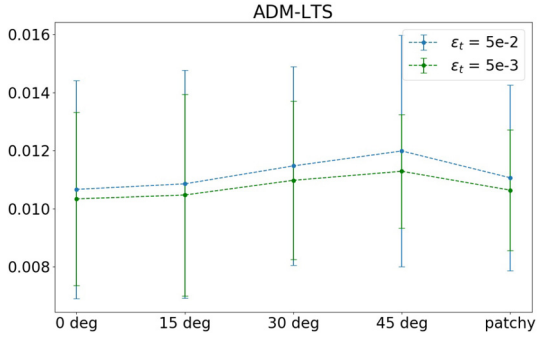

Fig. 33. Test case 6 - Mean and standard deviation errors of the saturation errors over 20 realization for the ADM-LTS method with different time threshold values respect to the reference solution $E_S = mean_{t=1}^{N_t}\left(mean|S_f(t) - S(t)|\right)$.

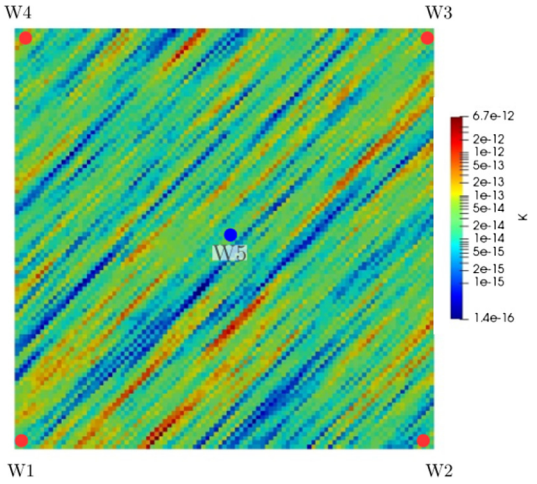

Fig. 34. Test case 7 - Base 10 logarithm of the permeability field.

5. Conclusions

A dynamic local space-time stepping scheme for transport in porous media (ADM-LTS) was devised and integrated within the sequentially-coupled multiphase flow-transport system. The studied coupled multiphase flow processed observe pressure and velocity change at every time step. The ADM-LTS method operates in two stages: first the solution is obtained at the coarsest space-time grid. Then this initial solution is improved by imposing an adaptive multi-resolution grid in space and time. The resolution of the space-time grid is defined based on an error criteria, with user-defined threshold values. This strategy also guarantees local mass conservation.

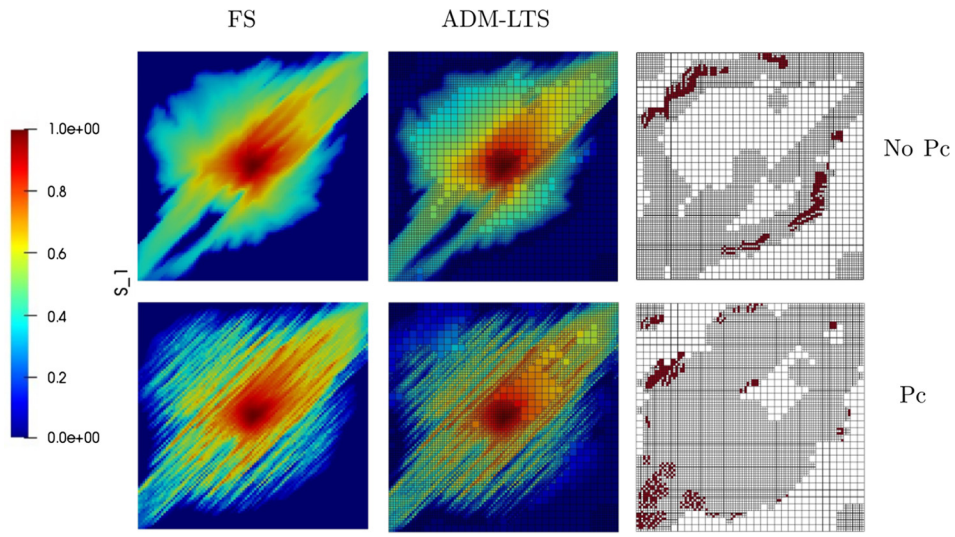

Fig. 35. Test case 7 - Reference solutions (left) and ADM-LTS saturation maps (right) without (top) and with (bottom) capillary heterogeneity effects.

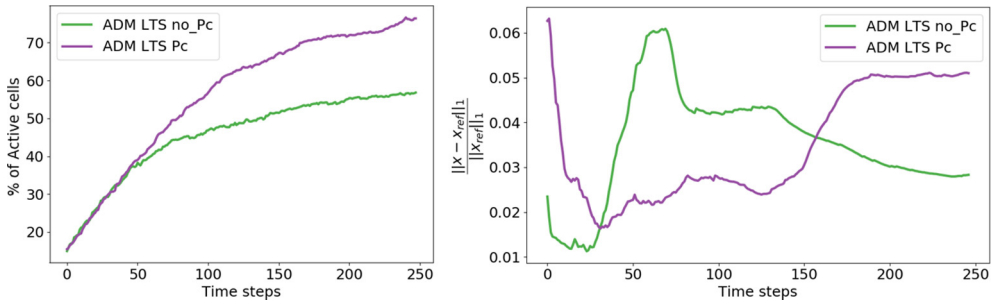

Fig. 36. Test case 7 - Number of active cells expressed as percentage of fine grid cells (left) and saturation relative errors in l^1-norm (right) for the ADM-LTS simulations.

Compared with the classical ADM approach, the ADM-LTS method employs coarse grids where high saturation gradients exist, but the phase velocity is nearly zero. This happens when the saturation front faces impermeable zones or barriers. The ADM-LTS grid resolution is decided implicitly by the mentioned two-stage strategy, where initially the coarsest space-time grid is used everywhere. Then, based on the introduced error criteria, the transport solution is locally improved with a multirate multilevel strategy on an adaptive space-time grid. This method is found promising to reduce the size of the system in the nonlinear loop without loss of accuracy.

Several numerical test cases with challenging transport physics were considered. Results showed that the ADM-LTS is promising for real-field applications. The research simulator (with all numerical test cases) is made available to the public (https://gitlab.com/darsim2simulator).

Future work includes development of enhanced prolongation operators to further improve the saturation quality at coarser levels (specially for slow-moving fronts). Another ongoing work is the implementation of ADM-LTS in the DARSim1 C++ research simulator for large-scale 3D test cases.

Declaration of competing interest

The authors declare that they have no known competing financial interests or personal relationships that could have appeared to influence the work reported in this paper.

Acknowledgements

Hadi Hajibeygi was funded by the 2019 Dutch National Science Foundation (NWO) grant, under Vidi scheme, with award number of 17509 (Project ADMIRE). Matteo Cusini was sponsored by the auspices of the U.S. Department of Energy by Lawrence Livermore National Laboratory (LLNL) under Contract DE-AC52-07NA27344. Authors thank Delft Advanced Reservoir Simulation (DARSim) research group members for the fruitful discussions during the development of the ADM-LTS method.

References

[1] D.R. Brouwer, J.D. Jansen, Dynamic optimization of water flooding with smart wells using optimal control theory, SPE J. 4 (2004) 391–402, https://doi.org/10.2118/78278-MS.

[2] R.J. de Moraes, J.R. Rodrigues, H. Hajibeygi, J.D. Jansen, Multiscale gradient computation for flow in heterogeneous porous media, J. Comput. Phys. 336 (2017) 644–663, https://doi.org/10.1016/j.jcp.2017.02.024.

[3] M. Cusini, R. Gielisse, H. Groot, C. van Kruijsdijk, H. Hajibeygi, Incomplete mixing in porous media: Todd-longstaff upscaling approach versus a dynamic local grid refinement method, Comput. Geosci. 23 (2) (2019) 373–397, https://doi.org/10.1007/s10596-018-9802-0.

[4] T.Y. Hou, X.-H. Wu, A multiscale finite element method for elliptic problems in composite materials and porous media, J. Comput. Phys. 134 (1) (1997) 169–189.

[5] P. Jenny, S. Lee, H. Tchelepi, Multi-scale finite-volume method for elliptic problems in subsurface flow simulation, J. Comput. Phys. 187 (1) (2003) 47–67.

[6] H. Hajibeygi, G. Bonfigli, M.A. Hesse, P. Jenny, Iterative multiscale finite-volume method, J. Comput. Phys. 227 (19) (2008) 8604–8621.

[7] H. Zhou, H.A. Tchelepi, et al., Two-stage algebraic multiscale linear solver for highly heterogeneous reservoir models, SPE J. 17 (02) (2012) 523–539.

[8] O. Møyner, K.-A. Lie, A multiscale restriction-smoothed basis method for high contrast porous media represented on unstructured grids, J. Comput. Phys. 304 (2016) 46–71, https://doi.org/10.1016/j.jcp.2015.10.010.

[9] M.J. Berger, J. Oliger, Adaptive mesh refinement for hyperbolic partial differential equations, J. Comput. Phys. 53 (3) (1984) 484–512, https://doi.org/10.1016/0021-9991(84)90073-1.

[10] B. Faigle, R. Helmig, I. Aavatsmark, B. Flemisch, Efficient multiphysics modelling with adaptive grid refinement using a mpfa method, Comput. Geosci. 18 (5) (2014) 625–636, https://doi.org/10.1007/s10596-014-9407-1.

[11] M. Cusini, C. van Kruijsdijk, H. Hajibeygi, Algebraic dynamic multilevel (adm) method for fully implicit simulations of multiphase flow in porous media, J. Comput. Phys. 314 (2016) 60–79, https://doi.org/10.1016/j.jcp.2016.03.007.

[12] M. Cusini, B. Fryer, C. van Kruijsdijk, H. Hajibeygi, Algebraic dynamic multilevel method for compositional flow in heterogeneous porous media, J. Comput. Phys. 354 (2018) 593–612, https://doi.org/10.1016/j.jcp.2017.10.052.

[13] J. Andrus, Numerical solution of systems of ordinary differential equations separated into subsystems, SIAM J. Numer. Anal. 16 (1979) 605–611.

[14] V. Savcenco, W. Hundsdorfer, J. Verwer, A multirate time stepping strategy for stiff ordinary differential equations, BIT Numer. Math. 47 (2007) 137–155.

[15] L. Delpopolo Carciopolo, L. Bonaventura, A. Scotti, L. Formaggia, A conservative implicit multirate method for hyperbolic problems, Comput. Geosci. 23 (4) (2019) 647–664, https://doi.org/10.1007/s10596-018-9764-2.

[16] L. Delpopolo Carciopolo, L. Formaggia, S. Anna, H. Hajibeygi, Conservative multirate multiscale simulation of multiphase flow in heterogeneous porous media, J. Comput. Phys. 404 (2020) 109134, https://doi.org/10.1016/j.jcp.2019.109134.

[17] P. Jenny, Time adaptive conservative finite volume method, J. Comput. Phys. 403 (2020), https://doi.org/10.1016/j.jcp.2019.109067.

[18] G.W. Thomas, D.H. Thurnau, Reservoir simulation using an adaptive implicit method, Soc. Pet. Eng. J. 23 (05) (1983) 759–768, https://doi.org/10.2118/10120-PA.

[19] D.A. Collins, L.X. Nghiem, Y.-K. Li, J.E. Grabonstotter, An efficient approach to adaptive-implicit compositional simulation with an equation of state, SPE Reserv. Eng. 7 (02) (1992) 259–264, https://doi.org/10.2118/15133-PA.

[20] J. Maes, A. Moncorgé, H. Tchelepi, Thermal adaptive implicit method: time step selection, J. Pet. Sci. Eng. 106 (2013) 34–45, https://doi.org/10.1016/j.petrol.2013.03.019.

[21] R. Helmig, Multiphase Flow and Transport Processes in the Subsurface: A Contribution to the Modeling of Hydrosystems, Environmental Engineering, Springer, 1997.

[22] Z. Chen, G. Huan, Y. Ma, Computational Methods for Multiphase Flows in Porous Media, vol. 2, Siam, 2006.

[23] M. Cusini, H. Hajibeygi, Algebraic dynamic multilevel (adm) method for simulations of multiphase flow with an adaptive saturation interpolator, in: ECMOR XVI-16th European Conference on the Mathematics of Oil Recovery, 2018.

[24] M. Christie, M. Blunt, Tenth SPE comparative solution project: a comparison of upscaling techniques, in: SPE Reservoir Simulation Symposium, 11-14 February 2001.

[25] N. Remy, A. Boucher, J. Wu, Applied Geostatistics with SGeMS: A User's Guide, Cambridge University Press, 2009.

[26] B. Li, S.M. Benson, Influence of small-scale heterogeneity on upward CO_2 plume migration in storage aquifers, Adv. Water Resour. 83 (2015) 389–404, https://doi.org/10.1016/j.advwatres.2015.07.010.